JTTEE5 21:550–560
DOI: 10.1007/s11666-011-9703-4
1059-9630/$19.00 © ASM International

Comparison of Oxidation and Microstructure of Warm-Sprayed and Cold-Sprayed Titanium Coatings

KeeHyun Kim, Seiji Kuroda, Makoto Watanabe, RenZhong Huang, Hirotaka Fukanuma, and Hiroshi Katanoda

(Submitted August 15, 2011; in revised form October 18, 2011)

Thick titanium coatings were prepared by the warm spraying (WS) and cold spraying (CS) processes to investigate the oxidation and microstructure of the coating layers. Prior to the coating formations, the temperature and velocity of in-flight titanium powder particles were numerically calculated. Significant oxidation occurred in the WS process using higher gas temperature conditions with low nitrogen flow rate, which is mixed to the flame jet of a high velocity oxy-fuel (HVOF) spray gun in order to control the temperature of the propellant gas. Oxidation, however, decreased strikingly as the nitrogen flow rate increased. In the CS process using nitrogen or helium as a propellant gas, little oxidation was observed. Even when scanning electron microscopy or an x-ray diffraction method did not detect oxides in the coating layers produced by WS using a high nitrogen flow rate or by CS using helium, the inert gas fusion method revealed minor increases of oxygen content from 0.01 to 0.2 wt.%. Most of the cross-sections of the coating layers prepared by conventional mechanical polishing looked dense. However, the cross-sections prepared by an ion-milling method revealed the actual microstructures containing small pores and unbounded interfaces between deposited particles.

Keywords cold spraying, ion milling, microstructure, oxidation, warm spraying, x-ray diffraction

1. Introduction

Thermal sprayed coatings are widely used to provide structural engineering materials with corrosion or wear resistance, lubrication, and thermal insulation in a broad spectrum of industries such as aeronautical, aerospace, chemical, electronics, iron and steel, paper and printing (Ref 1, 2). In conventional thermal spray processes, it is necessary to heat up and melt the feedstock materials in the form of either powder or wire to high temperature above the melting point to deposit a coating. The melted or semi-melted state often causes deleterious effects such as oxidation, undesirable phase transformation, and high residual stress in the coating layer, as well as heating of the substrate (Ref 3). Kinetic spraying processes such as cold spraying (CS) and warm spraying (WS) in which the powder is sprayed and deposited in a solid state can minimize or eliminate such detrimental effects (Ref 3-5). Figure 1 shows schematic diagrams of CS and WS processes. In CS, a supersonic jet of compressed process gas such as nitrogen or helium passes through a DeLaval type nozzle, accelerates small size (1-50 μm) particles to a high velocity (300-1200 m/s) and facilitates the deformation of particles upon impact (Ref 3, 4, 6). In contrast, WS uses a supersonic flow of combustion gas made from a mixture of fuel and oxygen (Ref 5). Moreover, the gas flow is mixed with an inert gas such as nitrogen in order to lower the temperatures of the gas and consequently the in-flight powder particles. The controlled gas flow accelerates and simultaneously heats the powder and makes a dense and tightly bonded coating. In WS process the aim is to heat the feedstock powder to higher temperatures compared to CS but below the melting point.

Several studies on WS and CS showed that the sprayed metallic powder particles impacted onto the substrate in a solid state are heavily deformed in a very short period, typically less than 10 ns, and well bonded to the substrate (Ref 3, 7, 8). Furthermore, the severe and nearly adiabatic plastic deformation generates heating of the impacted region and forms very fine grains with the size of several tens of nanometers within the particles (Ref 7, 9). It is suggested that the grain refinement results from in situ dynamic recrystallization during spraying. In addition, the

This article is an invited paper selected from presentations at the 2011 International Thermal Spray Conference and has been expanded from the original presentation. It is simultaneously published in *Thermal Spray 2011: Proceedings of the International Thermal Spray Conference*, Hamburg, Germany, September 27-29, 2011, Basil R. Marple, Arvind Agarwal, Margaret M. Hyland, Yuk-Chiu Lau, Chang-Jiu Li, Rogerio S. Lima, and André McDonald, Ed., ASM International, Materials Park, OH, 2011.

KeeHyun Kim, National Institute for Materials Science (NIMS), Tsukuba, Japan; and University of Birmingham, Birmingham, United Kingdom; **Seiji Kuroda** and **Makoto Watanabe**, National Institute for Materials Science (NIMS), Tsukuba, Japan; **RenZhong Huang** and **Hirotaka Fukanuma**, Plasma Giken Co. Ltd., Oosato, Japan; **Hiroshi Katanoda**, Kagoshima University, Korimoto, Japan. Contact e-mails: K.Kim.2@bham.ac.uk and Kuroda.seiji@nims.go.jp.

impact-heating can induce oxidation of sprayed particles forming very thin oxide films of the nanometer scale (Ref 8). However, there has been no systematic study on the effects of temperature and velocity of sprayed powder particles on the microstructure as well as on their oxidation in WS and CS. In this study, the microstructure and oxidation of titanium coatings sprayed by WS and CS are compared because of the high reactivity of the metal with oxygen and superb properties such as corrosion resistance.

2. Experimental Procedure

2.1 Materials and Spraying Conditions

Prior to spraying powder particles, the temperature and velocity of in-flight spherical titanium particles in WS and CS were numerically calculated along the axial trajectory by gas dynamics modeling (Ref 5). The detailed calculations were explained in previous papers (Ref 10, 11) and briefly summarized in Section 3.1. Based on the data, commercially available titanium powder (TILOP-45 μm, Sumitomo, Tokyo, Japan) was used to make coatings. The powder had a Gaussian powder size distribution from 1 to 45 μm with a volume average of 28 μm and a nearly spherical morphology (Ref 7, 12). The same titanium powders were sprayed on steel substrates (JIS S45C) by CS using nitrogen or helium as processing gas or by WS. In WS, nitrogen gas flow in the range of 0.5-2.0 m^3/min was used to control the temperature of feedstock powder. The spraying parameters of WS and CS used in this study are summarized in Table 1. The spraying system for CS is an axial injection high pressure cold spray system (PCS-1000, Plasma Giken Co. Ltd., Japan) and the system for WS is modified from commercial high velocity oxy-fuel (HVOF) spraying equipment (Ref 5). The coating thicknesses were about 300-400 μm.

2.2 Coating Characterization

As-sprayed coatings of WS or CS samples were used to obtain x-ray diffraction patterns (XRD). The XRD patterns were recorded by an x-ray diffractometer (RINT 2500, XRD-Rigaku Corp., Japan) from 20° to 80° using Cu Kα (λ = 0.154056 nm) and calibrated by the background

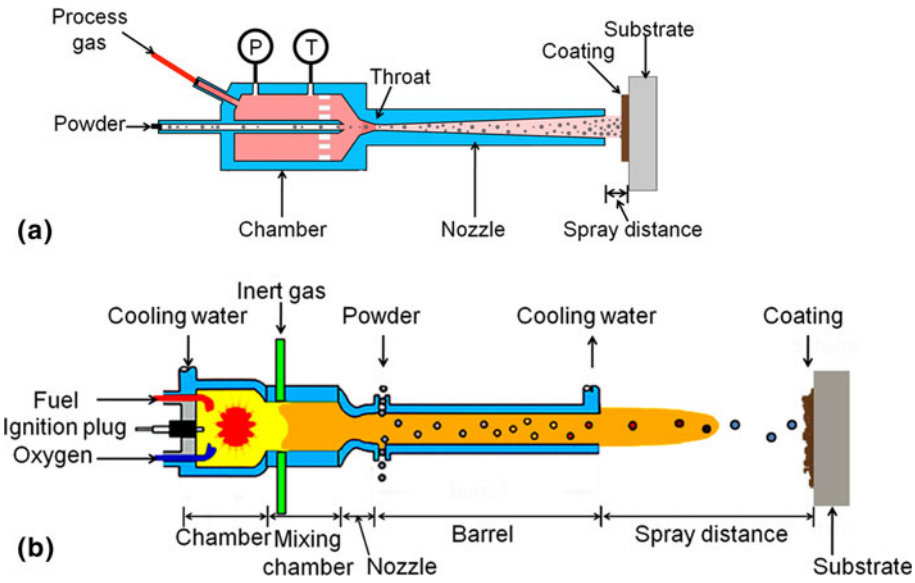

Fig. 1 Schematic diagrams of CS (a) and WS (b) process

Table 1 Spraying conditions in WS and CS processes

Sample	Process	Fuel, dm^3/min	Oxygen, m^3/min	Process gas				Powder feeding rate, g/min	Spray distance, mm	Spray pass	Gun transverse speed, mm/s
				Gas	Pressure, MPa	Temp., K	Flow rate, m^3/min				
WS1	Warm	0.39	0.81	Nitrogen			0.50	40	180	7	700
WS2	Warm	0.35	0.71	Nitrogen			1.00	40	180	7	700
WS3	Warm	0.30	0.62	Nitrogen			1.50	40	180	7	700
WS4	Warm	0.27	0.55	Nitrogen			2.00	40	180	7	700
CS5	Cold			Nitrogen	2.0	673	1.22	30	20	2	500
CS6	Cold			Nitrogen	4.0	1073	1.95	30	20	2	500
CS7	Cold			Helium	2.0	673	2.97	30	20	2	500
CS8	Cold			Helium	3.2	673	4.73	30	20	2	500

noise level as a reference in a Jade-6 software. Cross-sections of WS and CS coatings were prepared vertically to their surfaces by a conventional mechanical polishing method using SiC sand papers and diamond suspensions. Then, a relatively new polishing method using a broad ion beam (Ref 13) was used to minimize the artifacts such as exaggerated densification and/or reduced porosity which can be induced by the plastic deformation of sprayed metallic powder particles during sample preparation. The broad ion beam milling was conducted in a commercially available apparatus called a cross section polisher (SM-09020CP, JEOL, Japan). The acceleration voltage and milling speed were 4 kV and 50 μm/h, respectively, under a chamber pressure of 2×10^{-3} Pa. Details of the ion beam milling method and principle are given elsewhere (Ref 13). The mirror polished and broad ion milled vertical cross-sections of the coatings were examined by a field emission scanning electron microscope (FE-SEM, JSM-6500, JEOL, Japan).

3. Results and Discussion

3.1 Calculated Temperature and Velocity of Gas and Particles in WS and CS

Figure 2 shows the calculated temperature and velocity of gas and in-flight powder with 30 μm diameter in WS and CS along the symmetry axis. Distance zero corresponds to the entrance to the diverging section of the nozzle in WS, whereas it corresponds to 100 mm in CS. In WS (Fig. 2a and b), the nozzle has a throat diameter of 7.9 mm and an exit diameter of 11 mm, followed by a 203 mm-long straight barrel. The assumption of chemical equilibrium state was employed in order to calculate the thermodynamic gas conditions in the combustion and mixing chambers. The gas velocity and temperature field from the nozzle to the barrel exit were calculated by numerically integrating Eq 1-4 (Ref 5) of the quasi-one-dimensional compressible flow, which take account of the change in the cross-sectional area of the gun, the friction in the barrel, and the heat loss to the cooling water through the inner wall of the barrel. The heat loss to the cooling water was determined experimentally (Ref 10) by measuring the flow rates and temperatures of the water at the inlet and outlet of the apparatus.

$$\frac{du_g}{dx} = \frac{u_g}{\left(M_g^2 - 1\right)A}\frac{dA}{dx} - \frac{u_g}{\left(M_g^2 - 1\right)}\left(\frac{\gamma M_g^2}{2}\frac{4f}{d} - \frac{\gamma - 1}{\gamma R T_g}\frac{\delta q}{dx}\right) \quad \text{(Eq 1)}$$

$$\frac{d\rho_g}{dx} = -\rho_g\left(\frac{1}{u_g}\frac{du_g}{dx} + \frac{1}{A}\frac{dA}{dx}\right) \quad \text{(Eq 2)}$$

$$\frac{dT_g}{dx} = -\frac{\gamma - 1}{\gamma R}\left(\frac{\delta q}{dx} + u_g\frac{du_g}{dx}\right) \quad \text{(Eq 3)}$$

$$p = \rho_g R T_g \quad \text{(Eq 4)}$$

where u_g is the gas velocity; M_g the gas Mach number; A the cross sectional area; γ the specific heat ratio; f the friction factor; d the barrel diameter; R the gas constant; q the heat loss per unit mass of gas; ρ_g the gas density; T_g the

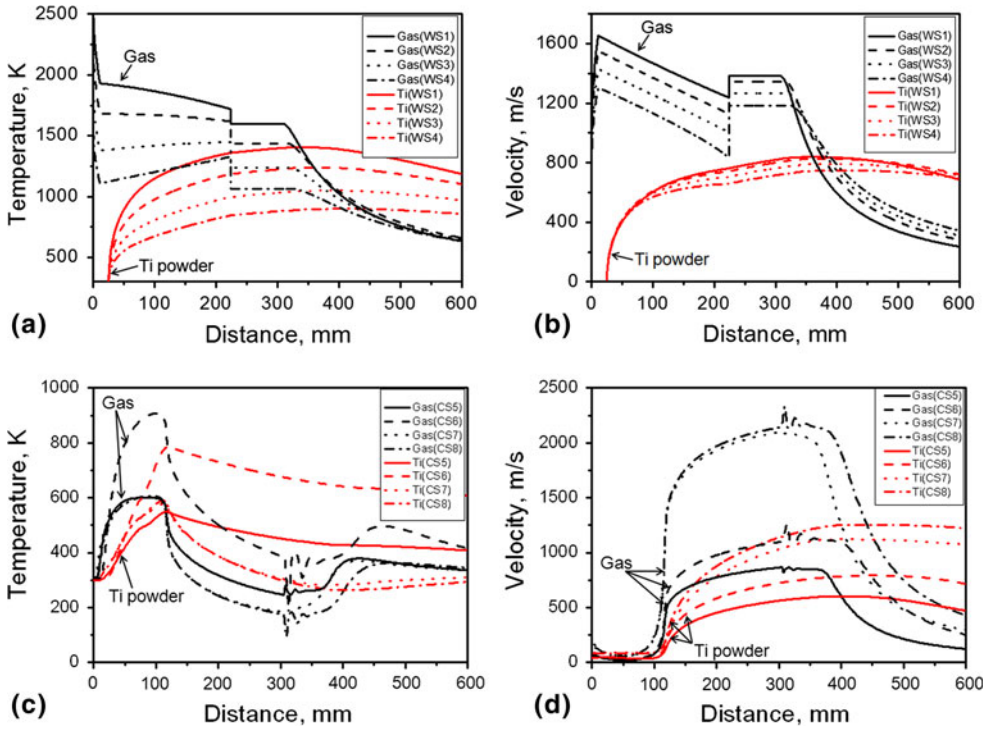

Fig. 2 The temperature (a, c) and velocity (b, d) of gas and titanium particles in WS (a, b) and CS (c, d) at the symmetry axis

gas temperature; and p is the static pressure. Semi-empirical equations (Ref 14, 15) were used to calculate the gas velocity and temperature outside the barrel along the center line. The under- and over-expansions of the jet flow were also modeled as stepwise changes in the gas velocity and temperature at the barrel exit by introducing a fully expanded jet Mach number (Ref 16), as will be shown later in Fig. 2(a) and (b). The gas velocity and temperature in the potential-core (Ref 16) region of the jet were set at constant values, which are calculated using a fully expanded jet Mach number. Once the gas flow field $u_g(x)$ and $T_g(x)$ are obtained, the velocity and temperature of a titanium spherical particle injected at the powder feed port can be, respectively, calculated by numerically integrating the equation of motion and the energy equation along the center line. Titanium powder is injected from the powder feed ports at the 25 mm position and accelerated by the combustion gas flow mixed with nitrogen. The barrel exit of the nozzle is located approximately at the 223 mm position. Inside the barrel, the gas velocity and temperature decreases gradually due to friction with the inner wall of the barrel and cooling (Ref 5), respectively, while the particle temperature and velocity increase rapidly. When the gas flow exits the barrel, the gas temperature and velocity changes stepwise due to the under-expansion of the jet flow (Ref 5). The jet temperature decay for $x > 350$ mm is slower in Fig. 2(a) compared to that which appeared in Ref 17. This is because a parameter to control the temperature decay of the jet was reviewed and modified after Ref 17, resulting in slower jet temperature decay. Since the particle temperature and velocity increase gradually and reach the highest point at about 403 mm, the substrate is placed on that position, i.e., the spraying distance from the exit of the barrel to the substrate is 180 mm in this study. As the nitrogen flow rate increases, it affects heavily the temperature of particles but not the velocity because the decreased gas velocity is compensated with the increased gas density resulting from the addition of nitrogen (Ref 5). Therefore, the particles are effectively accelerated to similar velocities and simultaneously heated to a wide range of temperatures by the controlled gas flow with nitrogen gas.

In CS (Fig. 2c and d), two-dimensional axisymmetric Navier-Stokes equations were solved numerically by the technique of computational fluid dynamics. As the process gas such as nitrogen or helium passes through the convergent-divergent part of the nozzle from 0 to 300 mm, the gas velocity increases continuously due to the fast gas expansion (Ref 11). Then, as the gas flow meets ambient air near the exit of the nozzle, the gas viscosity induces slightly an increase of temperature and decrease of velocity of the gas flow (Ref 11). The particle temperature and velocity show a similar increase and decrease with those of the gas flow. After the throat of the nozzle, however, the temperature of particles decreases at a rate slower than that of the gas and the velocity of particles increases continuously due to much higher density of particles than that of the gas. It should be noted that before the particles flow into the convergent-divergent part of the nozzle their temperatures are close to the gas temperature, which may induce dynamic oxidation of in-flight particles at the nanometer scale (Ref 8). Considering the temperature and velocity of particles including the bow shock of processing gas which can reduce particle impact velocities (Ref 18), the substrate is placed at the position of about 320 mm. Consequently, the spraying distance from the exit of the barrel to the substrate is 20 mm in this study.

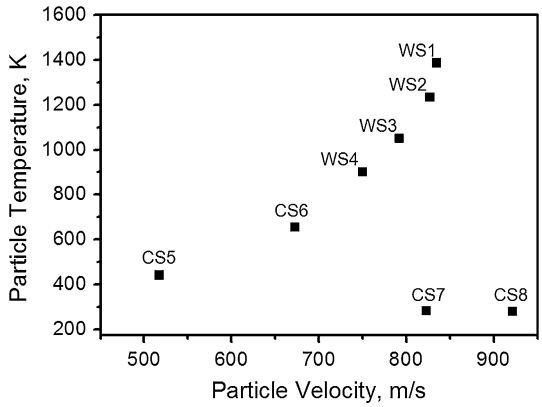

Fig. 3 Temperature and velocity of in-flight titanium powder particles at the spraying distance 180 mm in WS and 20 mm in CS before impacting the substrate

The temperature and velocity of in-flight titanium powder particles in this study are summarized in Fig. 3, which were calculated at the spraying distance of 180 mm in WS and 20 mm in CS, respectively, before impacting on the substrate. Using helium as a processing gas, the velocity of in-flight particles is the highest in this study under the CS8 condition, while the temperature of particles is the highest in the WS1 condition.

3.2 XRD Patterns of WS and CS Coating Samples

Figure 4 shows the XRD patterns of WS and CS samples. The coatings (WS1 and WS2) that were sprayed with particles heated to high temperatures show some peaks corresponding to titanium oxide, such as TiO. As the temperature of in-flight powder particles in WS is decreased from about 1400 to 1050 K, the oxide peaks gradually decrease in intensity and finally disappear in the WS3 sample. No noticeable oxides are detected in the WS3-4 and CS5-8 samples. Therefore, the solid-state spraying and bonding formation in the samples can minimize or eliminate the detrimental effects, such as severe oxidation, of sprayed metallic materials of conventional thermal spraying processes using a melted or semi-melted state. In the XRD patterns, there are also not any recognizable peaks corresponding to the β phase, which is the high temperature phase of titanium (Ref 19). Our previous studies using high resolution transmission electron microscopy also showed the absence of β phase in a single deposited particle (Ref 7) even though the rapid quenching effect of approximately 10 K/s in the spraying process (Ref 20, 21), if it occurred, might have induced the martensitic phase transformation from β phase and resultant fine platelet structure. Therefore, the temperature of the sprayed particles might not reach the martensitic

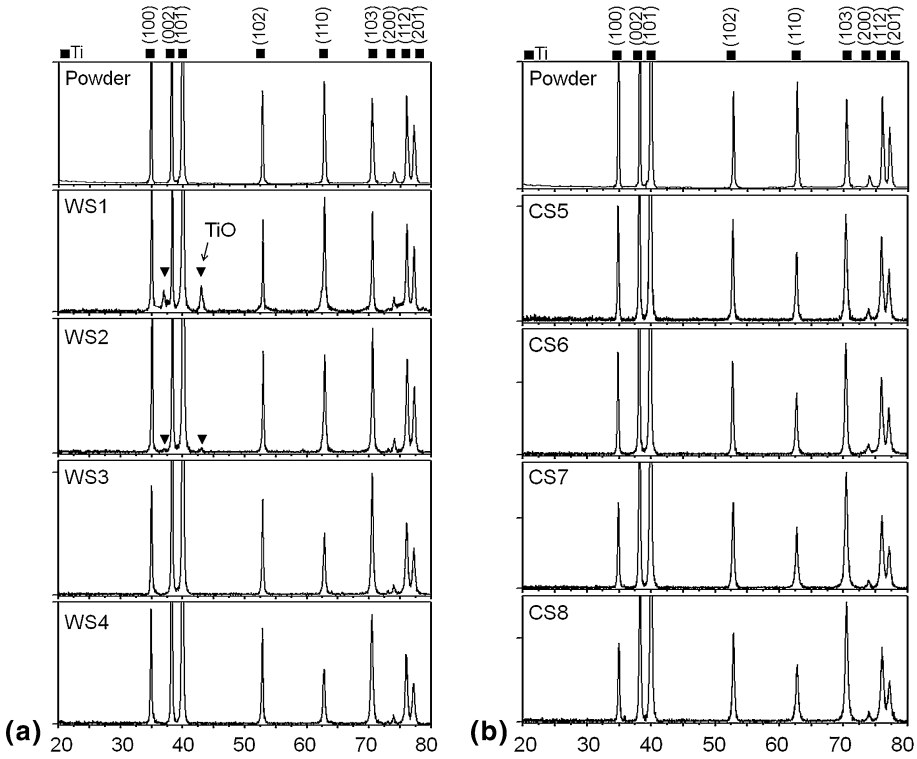

Fig. 4 XRD patterns of WS (a) and CS (b) samples

transformation temperature of titanium (Ms, 1128 K) (Ref 19) though the calculated temperature of the in-flight powder in Fig. 2 exceeded it, or the extreme heating and cooling rate might restrain any transformation during spraying (Ref 22). There is another possibility that even though β phase could form, the successive impact of numerous sprayed particles during the spraying process to make a coating layer might induce an annealing effect of previously deposited particles. As a result, the β phase of titanium was not detected in the XRD analysis or observed in the cross sectional microstructure of titanium coating layer produced by WS (Ref 23) or CS (Ref 24-32). As our previous studies already showed (Ref 33, 34), in this study any detectable peaks of titanium nitride such as TiN are also not observed due to the high affinity of titanium to oxygen.

Severe plastic deformation of metals induces appreciable changes in the line shape and intensity of diffracted x-rays (Ref 35). The broadening in sprayed titanium coatings is mainly produced by particle (or crystallite) size and/or lattice strain. The particle size induced broadening effect of the peak full width at half maximum (FWHM) is estimated from the Scherrer formula (Ref 36).

$$d_s = \frac{0.9\lambda}{B\cos\theta},$$

where d_s is the particle size in the Scherrer formula; λ the wavelength; B the FWHM of XRD peaks in radians; and θ is the angle at peak position. As the crystal size decreases, the diffraction curve becomes broader. Using the observed FWHM of the coatings, the particle size in the samples was estimated and summarized for a main crystallographic plane of (101) in Table 2. It is worth noting that the Scherrer formula is based on an assumption that the peak broadening is caused by the crystal size effect only. In addition, the amount of strain distribution (non-uniformity) in samples may induce the broadening of the FWHMs. The non-uniform strain induced broadening effect of the FWHM is estimated by the Williamson and Hall (WH) plot that is obtained by comparing the trend line equation (Ref 24, 35, 37).

Table 2 Measured FWHM, particle size (d_s) for the main (101) plane determined by Sherrer formula and strain distribution (ε) in samples

Sample	FWHM	d_s	ε (×10^{-3})
WS1	0.23	37	1.6
WS2	0.24	35	2.1
WS3	0.26	33	1.5
WS4	0.27	31	3.6
CS5	0.26	32	6.9
CS6	0.25	33	6.6
CS7	0.29	28	7.2
CS8	0.30	28	8.1

$$\varepsilon = \frac{\beta\cos\theta - A}{2\sin\theta},$$

where A is expressed as $C\lambda/d_w$ where C is the correction factor (~1) and d_w is the particle size in the WH plot, and ε is the strain. In a plot of $\beta\cos\theta$ vs. $\sin\theta$ (Ref 37), the slope and the intercept with the y-axis give the strain and the

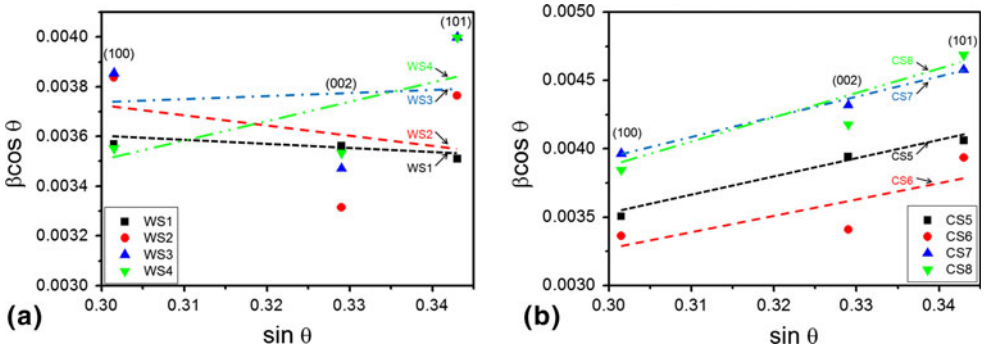

Fig. 5 WH plot for WS (a) and CS (b) samples

crystal size, respectively, as shown in Fig. 5. The amount of non-uniform strain distribution in each sample is summarized in Table 2. Compared to the strain (6-7 $\times$ 10^{-4}) in as-received powder, strain exists in all coating samples, which indicates straining during the spraying processes. Furthermore, the CS samples that were sprayed at high velocity but not thermally softened during the process have slightly higher levels of strain than those in the thermally softened WS samples which were heavily deformed and annealed in a short time by the operating spray gun during the coating process. However, the value of strain ($<$0.1%) in each sample is quite small. Therefore, the broadening of FWHMs in Fig. 4 is mainly due to the crystal size. In this study, the particle sizes obtained from the Scherrer formula are consistent with those obtained by the WH plot only for 3 WS samples (38 nm for WS1, 30 nm for WS2, and 45 nm for WS3) but inconsistent for the rest of the samples, i.e., WS4 (214 nm) and all CS samples, although the grain sizes acquired by the two methods were similar (Ref 24), which remains as a matter to be discussed further. Nevertheless, the estimated particle size of about 30 nm by the Scherrer method in Table 2 is in good agreement with the observed grain size (10-50 nm) of warm sprayed titanium powder particles (Ref 7, 12). However, since many successive powder particles are deposited onto and deform previously deposited particles in a coating process to make a thick coating layer the successive impacts can induce the re-grain refinement of recrystallized fine grains in the previously deposited particles (Ref 38). Therefore, the estimated grain size in XRD analysis may result from the grain growth at the nanometer scale of fine grains due to the heating(s) induced by the severe plastic deformation in the impacted regions and/or by the spraying gun. Figure 6 shows the 3-D plot of temperature, velocity and grain size in XRD analysis. It is clearly shown that as the temperature of in-flight particles decreases and simultaneously their velocity increases the finer grains form. It must be noted, however, that in case of low temperature and high velocity, i.e., the CS8 case in this study, the grain refinement occurred in a limited region along the interface of substrate/particle or particle/particle because the driving force for recrystallization is low at low temperature (Ref 17). Therefore, it is believed that there is a critical temperature and velocity to form a uniform microstructure composed of very fine grains.

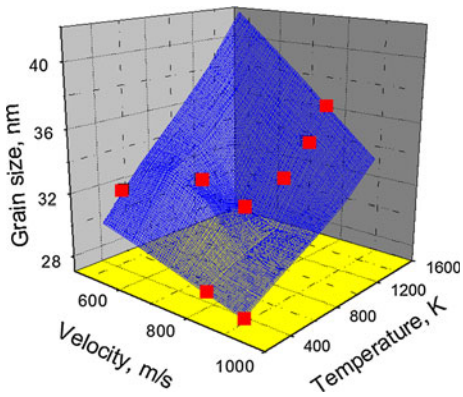

Fig. 6 3-D plot of velocity, temperature, and grain size in XRD analysis

The relative intensity of the (103) plane in Fig. 4 is found to increase with increasing the particle temperature and/or velocity in WS or CS samples, while the relative intensities of (100) or (110) planes decrease. Similarly, in Fig. 5, as the temperature of in-flight particles increases, the peak broadenings of FWHM in (100) and/or (002) planes are clearly observed. The changes in the peak intensities and the broadening result from a recrystallization process inducing the formation of fine grains of severely deformed coating layers (Ref 7, 9, 35, 36).

3.3 Microstructure of Titanium Coatings in WS and CS

Figure 7 shows SEM images of conventional mechanically polished thick coatings deposited by WS and CS. A sample made by HVOF spraying was added in order to compare the microstructure. The spraying conditions using a TAFA JP-5000 HVOF system (Praxair, USA) were 203 mm barrel, 360 mm spraying distance, 700 mm/s gun transverse speed, 0.51 dm^3/min fuel and 1.8 m^3/min oxygen. In the HVOF sample, since melted particles during spraying are easily oxidized due to the high oxygen affinity of titanium, gray boundaries composed of titanium and oxygen are observed with dark contrast in BSE (backscattered electron) image (see also Fig. 8). In WS1, with the lowest flow rate of 0.5 m^3/min, the gray

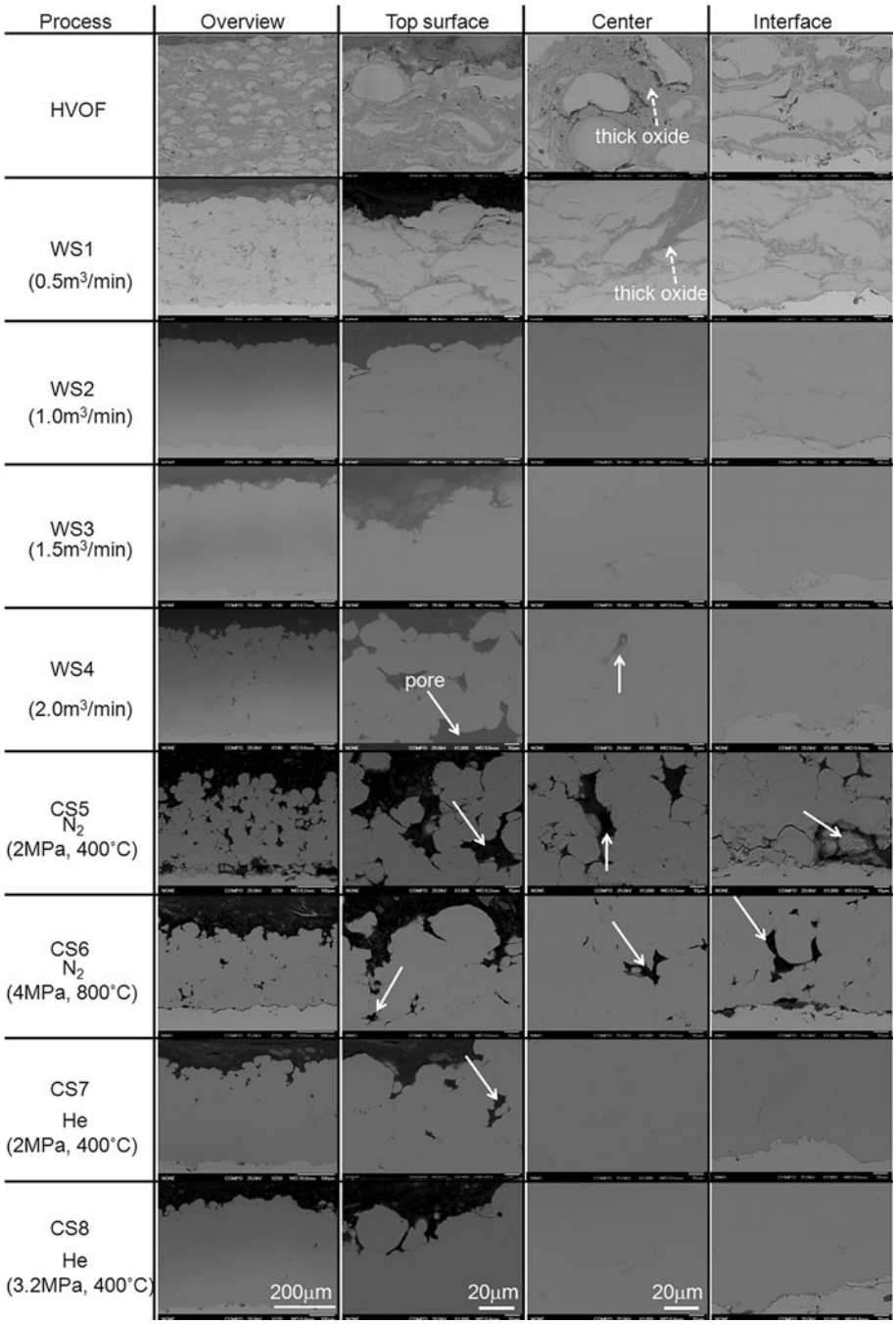

Fig. 7 Cross-sectional backscattered electron micrographs of titanium coatings fabricated by HVOF, WS and CS. The vertical cross sections were prepared by a conventional mechanical polishing method. The dotted or solid arrows indicate thick oxides or pores

boundaries are also observed. The oxide boundaries act as a barrier across the interfaces prohibiting the intimate bonding between particle and substrate or particles. As a result, the adhesive strength of the coating was lower than that of other coatings made at higher nitrogen flow rates (Ref 8, 33). However, as the flow rate increases, recognizable gray boundaries disappear in SEM images. In addition, the titanium coating layers obtained at 1.0 (WS2) and 1.5 m^3/min (WS3) look highly dense due to the low oxidation and sufficient deformation of sprayed particles. At a flow rate of 2.0 m^3/min (WS4), the coating becomes porous due to relatively low temperature and velocity, which results in insufficient deformation of sprayed particles. In CS5 using nitrogen as processing gas, the coating is very porous and not well bonded to the steel substrate. As a result, the coating layer was easily delaminated during sample preparation for SEM observation due to weak bonding between the coated layer and the substrate.

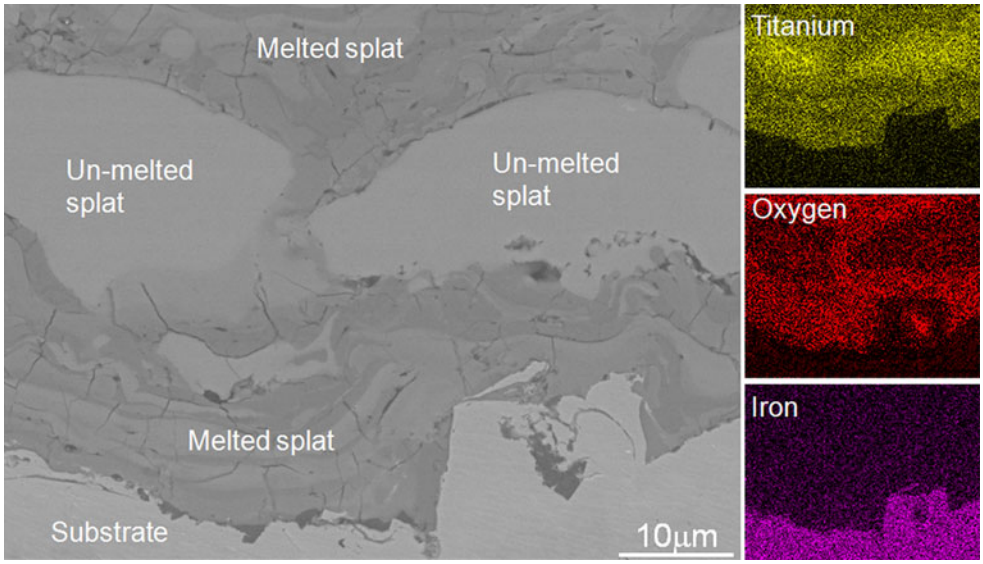

Fig. 8 Cross-sectional backscattered electron micrographs of titanium coating composed of melted and un-melted splats and corresponding SEM-EDX element mappings of titanium, oxygen, and iron

CS6 sample shows also porous microstructure, which is slightly similar to WS4. However, when helium (CS7 and CS8) was used, the coatings look highly dense due to the high velocity of sprayed particles resulting in high kinetic energy and consequently heavy deformation even though the temperatures were very low.

As already suggested in a recent paper (Ref 13), metallographic sample preparation for SEM observations is often problematic because during grinding and polishing plastic deformation of sprayed metallic particles can induce a denser microstructure than the actual. WS3 and CS8 coatings which looked highly dense in this study were ion-milled to examine the extent of exaggerated densification of the coating layers. Figure 9 shows SEM images of ion-milled cross sections of WS3 and CS8 samples. Compared with the mechanically polished cross sections in Fig. 7, the ion-milled samples are slightly more porous. Especially, a somewhat porous microstructure is observed even near the interface of the coating/substrate where many successive particles impacted previously deposited particles and consequently it is thought that the region should be highly dense. In a coating process, a variety of particle sizes are used to make a thick layer and many particles impact onto previously deposited particles at different angles. These various sizes and impacting angles induce pores among the particles. For instance, two laterally impacted particles can make a void under their jetting regions as shown in a previous paper (Ref 38). If a large particle impacts the region, it can deform and press down the void and consequently the void disappears or is reduced. If a small particle impacts, however, it does not have the same effect and consequently pores remain in a coating layer, as indicated in Fig. 9 by arrows.

The SEM images in Fig. 7 and 9 as well as XRD peaks in Fig. 4 showed that some oxides only exist in the coating layers of WS1-2 samples. It is worth mentioning, however, that a recent investigation using TEM (transmission electron microscopy) showed a nanometer-sized oxide layer which was formed by dynamic oxidation in WS3 samples (Ref 8). Therefore, it is essential to study more precisely the oxygen content in coating layers.

3.4 Oxygen Contents of WS and CS Coating Samples

The oxygen contents in WS1-CS8 coating samples were analyzed by the inert gas fusion method (Ref 23). Figure 10 shows the measured oxygen content in each sample. In WS1 sample, titanium powder particles were heavily reacted with the gas environment during spraying because their temperature was high enough to induce severe oxidation. It was shown that the parabolic rate law of oxidation in the temperature range of 600-1650 K can be applied at the initial stage of oxidation (Ref 5). Consequently, the oxygen content of about 5.3 mass% in WS1 coating is much higher than any of the other samples in this study. As the nitrogen flow rate increases from 0.5 to 1.0 m^3/min, the oxygen content decreases significantly due to the lower flame temperature (Ref 5). At higher nitrogen flow rate of 1.5 or 2.0 m^3/min, the oxygen content decreases further to 0.25 or 0.22 mass%. In CS coating samples, the oxygen contents are low regardless of the temperature and pressure of the processing gas, such as nitrogen or helium in this study. However, an important point to emphasize is the fact that even though the oxygen contents in the WS3-4 and CS5-8 samples are low, the oxygen content of these coatings clearly increased than that of the feedstock powder. Several studies have suggested that the surface oxide of metallic powder can be easily broken and removed by severe deformation induced by the shear instability, which means a local overwhelming of thermal softening over work hardening (Ref 3, 4, 20, 21, 39, 40). As a result, the oxygen contents may decrease in the coatings. In this study, however, the oxygen contents

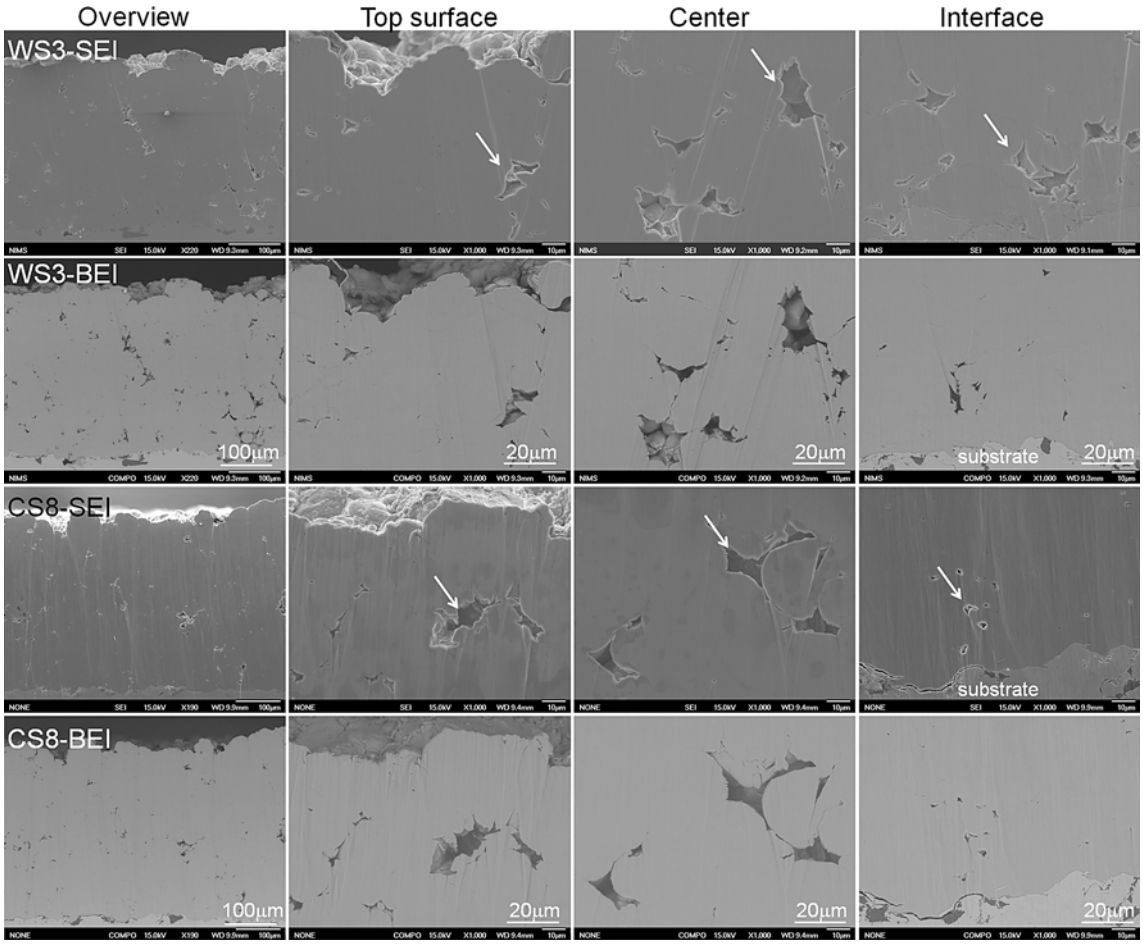

Fig. 9 Ion-milled vertical cross-sections of WS3 and CS8 samples. SEI and BEI are secondary electrons and backscattered electrons images, respectively. The arrows indicate pores in coating layers

increased slightly even in CS samples using helium gas. Since titanium can dissolve oxygen up to about 13 wt.% (Ref 41), it is necessary to know where the oxygen exists in the coating layers in order to understand and predict their potential mechanical properties. Kim et al. showed by high resolution energy-filtered TEM analysis that most of the oxygen exists near the interface of the substrate/particle or particle/particle because the dwell time at the temperature for the diffusion of oxygen into the titanium matrix is too short in the WS process (Ref 34, 38). Furthermore, Balani et al. evidently showed that the oxide layer of metallic powder exists in the interface of splats even in the CS process using helium gas (Ref 39, 40). In addition, Kim and Kuroda also showed that the surface oxide is not clearly removed by the impact of another particle onto a previously deposited one at the atomic scale and furthermore new oxide can be formed on the surface during spraying (Ref 8). These results indicate that the severe deformation of sprayed particles may not remove completely the oxide(s) covering the surface of metallic powder in WS and/or CS. Consequently, the oxide may influence the bonding formation of sprayed particles and the resultant mechanical properties.

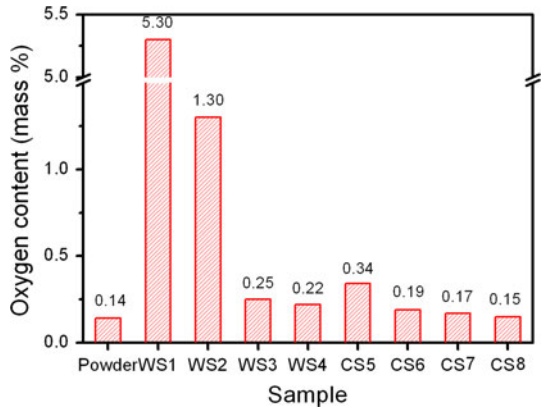

Fig. 10 Measured oxygen contents in WS and CS samples by the inert gas fusion method

4. Summary

The same commercially available titanium powder particles were sprayed by the WS or CS process, respectively. In WS, the temperature and velocity of in-flight

particles were effectively controlled by nitrogen gas in the mixing chamber. As a result, the particles impacted the substrate in a solid state in high nitrogen flow rates. In CS, the temperature and velocity were controlled by the pressure and temperature of nitrogen or helium propellant gas.

In WS, thick oxides were formed from the melted particles during spraying under the low nitrogen flow rate conditions. As the nitrogen flow rate increased, however, notable oxides were almost eliminated but the porosity of the coating layer increased due to the lack of deformation of particles under the highest flow rate condition. On the contrary, in CS, significant oxides were not observed regardless of the propellant gases. However, when nitrogen gas was used, the coating layers were porous due to relatively low gas density and resultant low velocity of sprayed particles, whereas helium created dense coating layers.

The ion-milled vertical cross-sections of warm sprayed and cold sprayed coating layers clearly showed that the coating layers were slightly porous even though they looked highly dense in the cross-sections prepared by the conventional mechanical polishing method.

In WS, the observed oxygen pickup increased with an increase in the temperature of the propellant gas and hence in the particle temperature. In CS, however, the oxygen content decreased with an increase in the temperature of the process gas for nitrogen. For highly reactive metal such as titanium, CS with high-pressure, high-temperature, and helium gas produced coatings with high density and low oxygen pickup of less than 200 ppm.

Acknowledgments

This research was supported by Nanotechnology Network program and World Premier International Research Center Initiative on Materials Nanoarchitectonics, MEXT, Japan, and KAKENHI 19360335.

References

1. N.P. Padture, M. Gell, and E.H. Jordan, Thermal Barrier Coatings for Gas-Turbine Engine Applications, *Science*, 2002, **296**(5566), p 280-284
2. L. Pawlowski, *The Science and Engineering of Thermal Spray Coatings*, 2nd ed., Wiley, New York, 2008
3. A. Papyrin, V. Kosarev, S. Klinkov, A. Alkhimov, and V. Fomin, *Cold Spray Technology*, Elsevier, Amsterdam, 2007
4. V.K. Champagne, *The Cold Spray Materials Deposition Process*, CRC Press, Boca Raton, 2007
5. S. Kuroda, J. Kawakita, M. Watanabe, and H. Katanoda, Warm Spraying—A Novel Coating Process Based on the High-Velocity Impact of Solid Particles, *Sci. Technol. Adv. Mater.*, 2008, **9**(3), p 033002
6. H. Fukanuma, N. Ohno, B. Sun, and R. Huang, In-Flight Particle Velocity Measurements with DPV-2000 in Cold Spray, *Surf. Coat. Technol.*, 2006, **201**(5), p 1935-1941
7. K. Kim, M. Watanabe, J. Kawakita, and S. Kuroda, Grain Refinement in a Single Titanium Powder Particle Impacted at High Velocity, *Scripta Mater.*, 2008, **59**(7), p 768-771
8. K. Kim and S. Kuroda, Amorphous Oxide Film Formed by Dynamic Oxidation During Kinetic Spraying of Titanium at High Temperature and Its Role in Subsequent Coating Formation, *Scripta Mater.*, 2010, **63**(2), p 215-218
9. K. Kim, M. Watanabe, and S. Kuroda, Thermal Softening Effect on the Deposition Efficiency and Microstructure of Warm Sprayed Metallic Powder, *Scripta Mater.*, 2009, **60**(8), p 710-713
10. H. Katanoda, T. Kiriaki, T. Tachibanaki, J. Kawakita, S. Kuroda, and M. Fukuhara, Mathematical Modeling and Experimental Validation of the Warm Spray (Two-Stage HVOF) Process, *J. Therm. Spray Technol.*, 2009, **18**(3), p 401-410
11. R.Z. Huang and H. Fukanuma, The Influence of Spray Conditions on Deposition Characteristics of Aluminum Coatings in Cold Spraying, *Thermal Spray 2009: Proceedings of the International Thermal Spray Conference*, B.R. Marple, M.M. Hyland, Y.C. Lau, C.J. Li, R.S. Lima, and G. Montavon, Ed., 2009, p 279-284
12. K. Kim, M. Watanabe, J. Kawakita, and S. Kuroda, Effects of Temperature of In-Flight Particles on Bonding and Microstructure in Warm-Sprayed Titanium Deposits, *J. Therm. Spray Technol.*, 2009, **18**(3), p 392-400
13. K. Kim, M. Watanabe, S. Kuroda, and N. Kawano, Observation of High Resolution Microstructures in Thermal Sprayed Coatings and Single Deposited Splats Using Ion Beam Milling, *Mater. Trans.*, 2011, **52**(3), p 439-446
14. G. Kleinstein, Mixing in Turbulent Axially Symmetric Free Jets, *J. Spacecr.*, 1964, **1**(4), p 403-408
15. P.O. Witze, Centerline Velocity Decay of Compressible Free Jets, *AIAA J.*, 1974, **12**(4), p 417-418
16. C.K.W. Tam, J.A. Jackson, and J.M. Seiner, A Multiple-Scales Model of the Shock-Cell Structure of Imperfectly Expanded Supersonic Jets, *J. Fluid Mech.*, 1985, **153**, p 123-149
17. S. Kuroda, M. Watanabe, K. Kim, and H. Katanoda, Current Status and Future Prospects of Warm Spray Technology, *J. Therm. Spray Technol.*, 2011, **20**(4), p 653-676
18. J. Pattison, S. Celotto, A. Khan, and W. O'Neill, Standoff Distance and Bow Shock Phenomena in the Cold Spray Process, *Surf. Coat. Technol.*, 2008, **202**(8), p 1443-1454
19. R. Boyer, G. Welsch, and E.W. Collings, *Materials Properties Handbook: Titanium Alloys*, ASM International, Materials Park, OH, 1994
20. H. Assadi, F. Gärtner, T. Stoltenhoff, and H. Kreye, Bonding Mechanism in Cold Gas Spraying, *Acta Mater.*, 2003, **51**(15), p 4379-4394
21. T. Schmidt, F. Gärtner, H. Assadi, and H. Kreye, Development of a Generalized Parameter Window for Cold Spray Deposition, *Acta Mater.*, 2006, **54**(3), p 729-742
22. T. LaGrange, G.H. Campbell, P.E.A. Turchi, and W.E. King, Rapid Phase Transformation Kinetics on a Nanoscale: Studies of the $\alpha \rightarrow \beta$ Transformation in Pure, Nanocrystalline Ti Using the Nanosecond Dynamic Transmission Electron Microscope, *Acta Mater.*, 2007, **55**(15), p 5211-5224
23. J. Kawakita, S. Kuroda, T. Fukushima, H. Katanoda, K. Matsuo, and H. Fukanuma, Dense Titanium Coatings by Modified HVOF Spraying, *Surf. Coat. Technol.*, 2006, **201**(3-4), p 1250-1255
24. C.K.S. Moy, J. Cairney, G. Ranzi, M. Jahedi, and S.P. Ringer, Investigating the Microstructure and Composition of Cold Gas-Dynamic Spray (CGDS) Ti Powder Deposited on Al 6063 Substrate, *Surf. Coat. Technol.*, 2010, **204**(23), p 3739-3749
25. C.-J. Li and W.-Y. Li, Deposition Characteristics of Titanium Coating in Cold Spraying, *Surf. Coat. Technol.*, 2003, **167**(2-3), p 278-283
26. T. Marrocco, D. McCartney, P. Shipway, and A. Sturgeon, Production of Titanium Deposits by Cold-Gas Dynamic Spray: Numerical Modeling and Experimental Characterization, *J. Therm. Spray Technol.*, 2006, **15**(2), p 263-272
27. K. Sakaki, T. Tajima, H. Li, S. Shinkai, and Y. Shimizu, Influence of Substrate Conditions and Traverse Speed on Cold Sprayed Coatings, *Thermal Spray 2004: Advances in Technology and Applications*, 2004, p 358-362
28. V. Shukla, G.S. Elliott, B.H. Kear, and L.E. McCandlish, Hyperkinetic Deposition of Nanopowders by Supersonic Rectangular Jet Impingement, *Scripta Mater.*, 2001, **44**(8-9), p 2179-2182
29. W.Y. Li, C. Zhang, H.T. Wang, X.P. Guo, H.L. Liao, C.J. Li, and C. Coddet, Significant Influences of Metal Reactivity and Oxide

Films at Particle Surfaces on Coating Microstructure in Cold Spraying, *Appl. Surf. Sci.*, 2007, **253**(7), p 3557-3562
30. S.H. Zahiri, C.I. Antonio, and M. Jahedi, Elimination of Porosity in Directly Fabricated Titanium via Cold Gas Dynamic Spraying, *J. Mater. Process. Technol.*, 2009, **209**(2), p 922-929
31. H.-R. Wang, B.-R. Hou, J. Wang, Q. Wang, and W.-Y. Li, Effect of Process Conditions on Microstructure and Corrosion Resistance of Cold-Sprayed Ti Coatings, *J. Therm. Spray Technol.*, 2008, **17**(5), p 736-741
32. T. Novoselova, P. Fox, R. Morgan, and W. O'Neill, Experimental Study of Titanium/Aluminium Deposits Produced by Cold Gas Dynamic Spray, *Surf. Coat. Technol.*, 2006, **200**(8), p 2775-2783
33. K.H. Kim, M. Watanabe, K. Mitsuishi, J. Kawakita, T. Wu, and S. Kuroda, Microstructure Observation on the Interface Between Warm Spray Deposited Titanium Powder and Steel Substrate, *Thermal Spray 2008: Proceedings of the International Thermal Spray Conference*, 2008, CD-ROM, p 1277-1282
34. K. Kim, M. Watanabe, K. Mitsuishi, K. Iakoubovskii, and S. Kuroda, Impact Bonding and Rebounding Between Kinetically Sprayed Titanium Particle and Steel Substrate Revealed by High-Resolution Electron Microscopy, *J. Phys. D Appl. Phys.*, 2009, **42**(6), p 065304
35. G.K. Williamson and W.H. Hall, X-Ray Line Broadening from Filed Aluminium and Wolfram, *Acta Metall.*, 1953, **1**(1), p 22-31
36. B.D. Cullity, *Elements of X-Ray Diffraction*, 2nd ed., Addison-Wesley, Menlo Park, CA, 1978
37. K.P. Misra, R.K. Shukla, A. Srivastava, and A. Srivastava, Blueshift in Optical Band Gap in Nanocrystalline $Zn_{1-x}Ca_xO$ Films Deposited by Sol-Gel Method, *Appl. Phys. Lett.*, 2009, **95**(3), p 031901-031903
38. K. Kim, S. Kuroda, and M. Watanabe, Microstructural Development and Deposition Behavior of Titanium Powder Particles in Warm Spraying Process: From Single Splat to Coating, *J. Therm. Spray Technol.*, 2010, **19**(6), p 1244-1254
39. K. Balani, A. Agarwal, S. Seal, and J. Karthikeyan, Transmission Electron Microscopy of Cold Sprayed 1100 Aluminum Coating, *Scripta Mater.*, 2005, **53**(7), p 845-850
40. M. Fukumoto, M. Mashiko, M. Yamada, and E. Yamaguchi, Deposition Behavior of Copper Fine Particles onto Flat Substrate Surface in Cold Spraying, *J. Therm. Spray Technol.*, 2010, **19**(1), p 89-94
41. P. Waldner, Modelling of Oxygen Solubility in Titanium, *Scripta Mater.*, 1999, **40**(8), p 969-974